PAPER

Check for updates

Bright aspects of defects and dark traits of dopants in the photoluminescence of $Er_2X_2O_7$:Eu^{3+} (X = Ti and Zr) pyrochlore: an insight using EXAFS, positron annihilation and DFT†

Santosh K. Gupta, [ID] *[ab] K. Sudarshan, [ID] [ab] Paramananda Jena, [ID] [c] P. S. Ghosh,[d] A. K. Yadav, [ID] [e] S. N. Jha[bf] and D. Bhattacharyya [ID] [be]

Understanding the intricacies and fundamental processes of materials involved in dopant- and defect-based luminescence is of paramount importance for scientists and engineers working towards the design of solid-state lighting, optoelectronics, scintillators, *etc.* The lack of such fundamental information has restricted the design of new oxide-based materials for light-emitting devices and phosphor-converted materials. Here, we have designed $Er_2Ti_2O_7$ (ETO), $Er_2Zr_2O_7$ (EZO), Eu^{3+}-doped ETO (EETO), and Eu^{3+}-doped EZO (EEZO) *via* high-energy ball milling. Structural analysis using X-ray diffraction (XRD) and Raman spectroscopy suggested the stabilization of the ordered pyrochlore structure for ETO and EETO, whereas EZO and EEZO are stabilized in the defect fluorite structure. The ETO and EZO samples exhibited bright blue emission under ultraviolet irradiation. X-ray absorption near edge structure (XANES) analysis completely rules out contributions from Ti^{3+} or Zr^{3+} to the host emission *via* confirming that they exist as tetravalent ions. Extended X-ray absorption fine structure (EXAFS) analysis confirms the presence of a high density of oxygen vacancies (OVs) near the Ti and Zr sites, respectively, in ETO and EZO. The DFT-calculated charge transition levels qualitatively explain the origin of the blue emission of ETO and EZO with the dominant involvement of ionized oxygen vacancies. Positron annihilation lifetime spectroscopy (PALS) suggested that few changes in the defect density or type occurred upon europium doping in EETO. The defect concentration and type change significantly in EEZO with respect to EZO, which is of significant importance due to the possible agglomeration of vacancies into large-size defect clusters in EEZO. Surprisingly, in both hosts, red/orange narrow emission from europium (585–750 nm, $^5D_0 \rightarrow {}^7F_J$) was completely absent. Density of state (DOS) calculations suggested that a possible reason for this is that the Eu f-states are dominantly distributed around the bottom edge of the valence band (VB), far from the Fermi energy, electronic band gap, and top edge of the VB actively participating in the electronic transitions. Similarly, the Eu f-states are distributed around the top edge of the conduction band, far from the electronic band-gap region. We believe this work will be quite helpful for selecting suitable hosts and dopants, band gap engineering, and defect tuning in the pursuit of achieving efficient host-to-dopant energy transfer in Eu^{3+}-doped pyrochlore materials.

1. Introduction

The discovery of more economic and sustainable novel materials with intriguing optical and structural properties has been attracting great attention in the global materials science community.[1–6] High-performance materials towards solid-state lighting, efficient phosphors, and nuclear waste hosts would serve as a boon to humanity in terms of providing cheap and

[a] Radiochemistry Division, Bhabha Atomic Research Centre, Trombay, Mumbai-400085, India

[b] Homi Bhabha National Institute, Anushaktinagar, Mumbai – 400094, India. E-mail: santoshg@barc.gov.in, santufrnd@gmail.com; Tel: +91-22-25590636

[c] School of Materials Science & Technology, Indian Institute of Technology (Banaras Hindu University), Varanasi-221005, Uttar Pradesh, India

[d] Glass and Advanced Materials Division, Bhabha Atomic Research Centre, Trombay, Mumbai-400085, India

[e] Atomic and Molecular Physics Division, Bhabha Atomic Research Centre, Trombay, Mumbai-400085, India

[f] Beamline Development & Application Section, Bhabha Atomic Research Centre, Trombay, Mumbai-400085, India

† Electronic supplementary information (ESI) available. See DOI: 10.1039/d0ma00978d

environmentally benign energy. $A_2B_2O_7$-type pyrochlore materials have shown tremendous potential in this direction as multifunctional materials for a variety of applications, particularly defect-induced photo/radioluminescence, catalysis, solid oxide fuel cells, and as a nuclear waste host.[7–9] Globally, there has been a gradual upsurge in research pertaining to defect- and dopant-induced luminescence in oxide lattices. However, a clear understanding of the origin of defect- and dopant-induced luminescence is still missing. As a result, there is a lack of motivation in designing new kinds of oxide-based optical materials.

Nuclear energy is one of the most green, clean and cheap sources of energy, and most countries are investigating it as an alternative to other conventional sources such as thermal, solar, hydel, etc.[10] The problem with nuclear energy is the high radioactivity associated with the used fuel, which can be very harmful to humanity because it is long-lived and highly radiotoxic.[11] Thus, most countries use a waste immobilization approach wherein the nuclear waste is immobilized in a glass matrix and stored under the earth's crust to remediate its harmful effects.[12] However, there are problems associated with the currently used borosilicate glass, such as low radiation stability and potential leaching of some of the components under high temperature and high pressure.[13] This is an undesirable situation and could lead to catastrophe if the waste enters the public domain. Thus, researchers worldwide have begun to look for an alternative to borosilicate glass. In this context, $A_2B_2O_7$ materials with various favourable properties, such as high radiation stability, negligible leaching, and the ability to accommodate large concentrations of lanthanides and actinides at both the A- and B-sites can be used as nuclear waste hosts.[14] $A_2B_2O_7$ compounds exist in two different structures, viz., the ideal pyrochlore (IP) and disordered fluorite (DF) structures, which have the space groups $Fd\bar{3}m$ and $Fm\bar{3}m$, respectively. The phase transition from the pyrochlore to the defect-fluorite structure is an order–disorder transition that is very sensitive to chemical composition and electronic configuration and can be induced by heating or irradiation.[14,15] IP is normally formed when the radius ratio falls between $1.46 \leq r(A^{3+})/r(B^{4+}) \leq 1.78$. On the other hand, when the radius ratio is less than 1.48, the DF phase is more likely to be stabilized. In other words, when the difference between the radii of the A and B ions is small, DF is the more favourable structure for $A_2B_2O_7$. The most important point to make here is that when the size difference between A and B is small, they can take up excess radiation by site-swapping and forming an antisite defect. Each structure has its own advantage; the IP structure is preferred for luminescence, thermal barrier coatings, and upconversion, whereas the DF structure is more suitable for nuclear waste hosts, catalysis, oxygen conductors in fuel cells, etc.[15] Moreover, the defect density will also be different in the two phases, which can have great implications on various properties such as magnetic, conductivity, and optical properties. Recently, we have explored $Nd_2Zr_2O_7$ and $Gd_2Zr_2O_7$, both of which exist in the DF structure, for self-activated emission, luminescence host and speciation of uranium.[16,17] Similarly, $La_2Zr_2O_7$ and $La_2Hf_2O_7$ pyrochlores, due to their $r(A^{3+})/r(B^{4+})$ ratios of greater than 1.46, exist in the IP structure, and have also been explored for use as phosphors, scintillators, thermal sensors, etc.[18]

In the present work, we have synthesized $Er_2Zr_2O_7$ (EZO) and $Er_2Ti_2O_7$ (ETO) using a solid-state method after ball milling of the constituent oxides. They are considered to be interesting pyrochlore materials and are used in a variety of applications, such as hydrogen storage,[19] magnetism,[20,21] ceramic pigments,[22] optical materials,[23] etc. Our aim was to stabilize both the IP and DF structures by changing the B-site element from Ti to Zr. We probed the structure and electronic states of ETO and EZO using synchrotron-based X-ray absorption spectroscopy (XAS), which comprises the X-ray near edge structure (XANES) and extended X-ray absorption fine structure (EXAFS) techniques. Both these structures have an abundance of defects, which can lead to interesting optical properties. Langlet et al. reported the temperature-dependent photoluminescence (PL) of an ETO thin-film, but were not able to clearly establish the origin of the photoluminescence, and their work was not focussed on visible spectroscopy.[23] The same group also carried out near-infrared PL spectroscopy of $Y_2Ti_2O_7$–$Er_2Ti_2O_7$ (YETO) films.[24] Saha et al. explored the PL of Er^{3+} in ETO.[25] However, all the above-mentioned works probed the infrared photoluminescence due to the Er^{3+} ion, and none probed defect-related visible emission in either EZO or ETO. We have probed the PL in undoped EZO and ETO and then corroborated the same using density functional theory (DFT) calculations. Because of their favourable properties, such as moderate phonon energy, wide band gap, structural/thermal stability, and the ability to accommodate a large concentration of lanthanide dopants, $A_2B_2O_7$ pyrochlores have traditionally been one of the most sought-after luminescence hosts. EZO and ETO pyrochlore systems are considered to be excellent hosts for PL owing to their high structural/thermal/chemical stability, ability to accommodate large dopants at both the A- and B-site, moderate phonon energy, and optimum band gap, dielectric constant and refractive index.[9,18] It is expected that upon doping them with europium ions, efficient red emission with high quantum yield, narrow emission and high color purity will be obtained. This expectation is based on the fact that both Er^{3+} and Eu^{3+} have same ionic charge and similar sizes, and hence, the doping should be efficient. In fact, doping an activator ion into a crystalline host has been found to be the most efficient strategy for designing advanced, superior and high-performance optoelectronic devices and light-emitting materials.[26–28] Despite this, there are no reports available in literature regarding the photoluminescence of lanthanide-doped EZO or ETO. Pokhrel et al.[29] reported the PL properties of $Er_2Hf_2O_7$:Eu^{3+}, but were unable to obtain any europium luminescence for reasons that were not clearly understood. Here, we have changed the lattice to EZO and ETO and doped them with Eu^{3+} (2.0 mol%) ions to see whether dopant luminescence would be achieved. In addition to the above-mentioned XAS and PL studies, powder XRD studies with Rietveld refinement and Raman studies have been carried out for structural characterisation of the samples, and positron annihilation lifetime studies have been carried out to study the defects. We believe that this work will provide a new dimension in understanding the defect- and dopant-induced luminescence in pyrochlore oxides

with a clear-cut design approach in terms of the dopant, choice of A/B site and vacancy tuning.

2. Experimental

The synthesis, instrumental details and theoretical methodology are discussed in the ESI,† as S1–S3.

3. Results and discussion

3.1. X-ray diffraction

The powder XRD patterns of undoped and Eu^{3+}-doped $Er_2Ti_2O_7$ and $Er_2Zr_2O_7$ are shown in Fig. 1A and B. The standard stick patterns of $Er_2Ti_2O_7$ and $Er_2Zr_2O_7$ are also given along with the respective XRD patterns for reliable comparison and ascertaining the phase purity. The prominent reflection planes are also marked in the figure. No additional peaks were found in the XRD patterns, confirming that the formed samples consisted of a single phase. The narrow peak profile suggests the highly crystalline nature of the undoped and Eu^{3+}-doped ETO and EZO.

It can be seen from the figure that $Er_2Ti_2O_7$ exhibits reflections corresponding to odd *hkl* planes due to the pyrochlore superlattice in addition to the fundamental fluorite reflections. The XRD pattern of the ETO sample could be modelled as the cubic system of pyrochlore with the $Fd\bar{3}m$ space group. Rietveld refinement of the XRD pattern of ETO was also carried out using the FULLPROF Suite. The Rietveld fitting of the XRD pattern of ETO, along with the residuals and Bragg reflections, is given in Fig. S1A (ESI†). The crystal structure of ETO with the $Fd\bar{3}m$ space group is given in Fig. S1B (ESI†). The quality of fit was evaluated based on χ^2. The lattice parameters from the Rietveld refinement of the XRD pattern of ETO are given in Table S1 (ESI†). The quality of the fit was found to be very good for both EZO and ETO, and the obtained fit factors such as the profile factor (R_p), weighted profile

factor (R_{wp}), expected weighted profile factor (R_{exp}) and reduced chi-square (χ^2) are tabulated in Tables S1 and S2 (ESI†). The structural parameters obtained are in good agreement with the reported literature.[21]

Unlike the XRD pattern of $Er_2Ti_2O_7$, the pattern of $Er_2Zr_2O_7$ shows peaks corresponding to only even *hkl* planes (Fig. 1B). This shows that the structure is the defect-fluorite-type with the space group $Fm\bar{3}m$. The two cations Er^{3+} and Zr^{4+} are disordered. The Rietveld refinement of the XRD profile of EZO is given in Fig. S2A (ESI†), along with the crystal structure of EZO with the $Fm\bar{3}m$ space group (Fig. S2B, ESI†). The structural parameters obtained from the Rietveld refinement of the XRD pattern of EZO are given in Table S2 (ESI†), along with the refinement parameters to indicate the quality of the fit.

The ionic radii of Er^{3+}, Ti^{4+} and Zr^{4+} are 100.4 pm (8 CN), 60.5 pm (6 CN) and 72 pm (6 CN), respectively. A smaller difference between the radii of the A and B cations in $A_2B_2O_7$ pyrochlores induces a degree of randomness between the cations of the A- and B-sites, leading to the formation of the defect fluorite type structure with the $Fm\bar{3}m$ space group. In the present case, $Er_2Ti_2O_7$, with an Er^{3+}/Ti^{4+} radius ratio of 1.659, is a pyrochlore with the $Fd\bar{3}m$ space group or with Er^{3+} and Ti^{4+} occupying the A- and B-sites of the pyrochlore. In the case of $Er_2Zr_2O_7$, the Er^{3+}/Zr^{4+} ratio is 1.394, and its crystal structure is observed to be of the defect-fluorite type *via* XRD. In ETO ($Er_2Ti_2O_6O'$) with the IP structure, Er, Ti, O and oxygen vacancies (OVs) are all arranged in an ordered arrangement. On the other hand, in EZO [$(Er/Zr)_4O_7$], the A/B as well as O/OV sites are all are arranged in a disorderly manner.

3.2. X-ray absorption near edge spectroscopy

The XAS spectra of $Er_2Zr_2O_7$ and $Er_2Ti_2O_7$ at the Er L3 edge are shown in Fig. 2a. The regions near the absorption edge (XANES regions) are shown in the inset of Fig. 2a. The edge position,
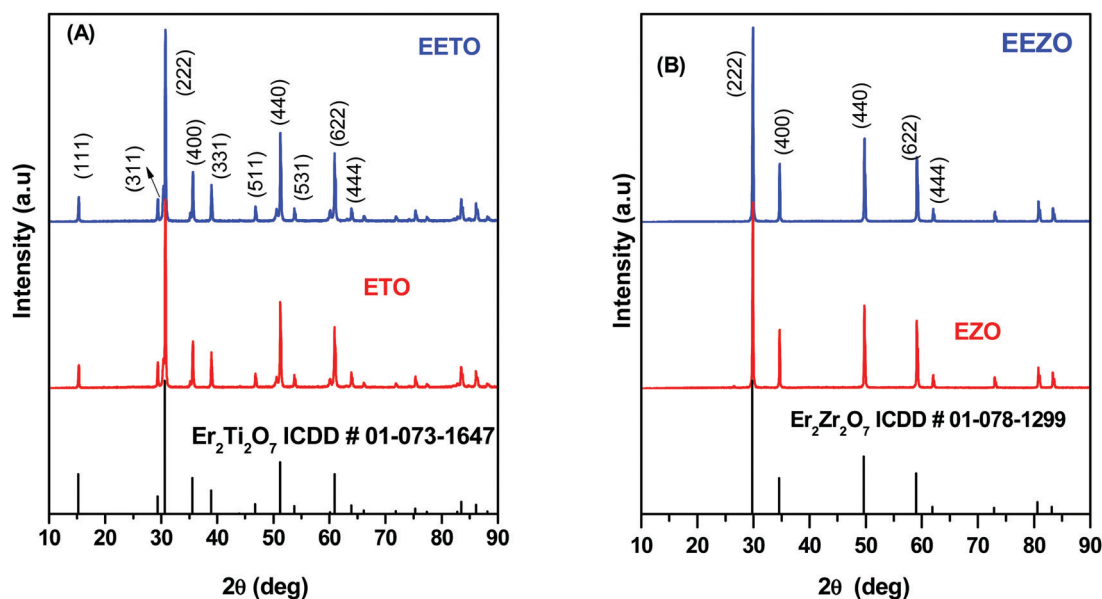

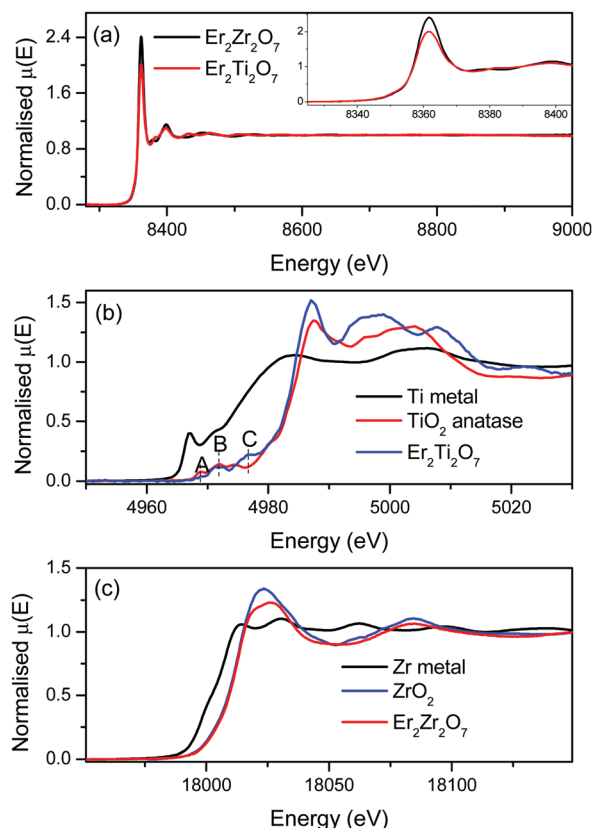**Fig. 1** Powder XRD patterns of undoped and Eu^{3+}-doped (A) $Er_2Ti_2O_7$ and (B) $Er_2Zr_2O_7$.

Fig. 2 (a) Normalised EXAFS spectra at the Er L3-edge; the inset shows the XANES region at the Er L3 edge. (b) The normalised XANES spectrum of $Er_2Ti_2O_7$ at the Ti K edge along with Ti metal and TiO_2 standards. (c) The normalized XANES spectrum of $Er_2Zr_2O_7$ at the Zr K edge along with Zr metal and ZrO_2 standards.

which gives the oxidation state of the absorbing atom, implies that Er is in same oxidation state in both $Er_2Zr_2O_7$ and $Er_2Ti_2O_7$. The normalized XANES spectrum at the Ti K edge of $Er_2Ti_2O_7$ are shown in Fig. 2b, along with Ti metal and TiO_2 (+4 state) standards. The absorption edge position of $Er_2Ti_2O_7$ is at the same position as that of TiO_2, suggesting that the Ti in the sample is in the Ti^{4+} oxidation state. The transition metal oxides show spectral features (pre-edge) immediately before the absorption edge due to the transition of 1s electrons to unoccupied states just below the continuum.[30] The pre-edge peaks are denoted as A, B and C in Fig. 2b. The pre-edge peaks A, B and C are attributed to the $1s-2t_{2g}$ and $1s-3e_g$ transitions in the octahedral field.[31] The normalised XANES spectrum of $Er_2Zr_2O_7$ at the Zr K edge is shown in Fig. 2c along with Zr metal foil and ZrO_2 standards. The edge position of $Er_2Zr_2O_7$ coincides with that of ZrO_2, suggesting that the Zr in the sample is in the Zr^{4+} oxidation state.

3.3. Raman spectroscopy

In the pyrochlores belonging to the $Fd\bar{3}m$ space group with the structure $A_2B_2O_6O'$, six Raman-active modes ($A_{1g} + E_g + 4F_{2g}$) were predicted by factor group analysis.[32,33] The Raman spectra of the ETO and EETO samples are shown in Fig. 3. The lower vibration modes are due to the vibration of Er–O and Ti–O
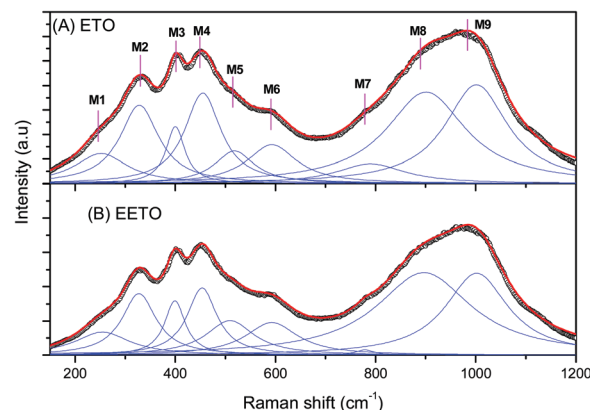

Fig. 3 Raman spectra of (A) undoped (ETO) and (B) Eu^{3+}-doped (EETO) $Er_2Ti_2O_7$. The open symbols represent the experimental data while the solid lines are fit to the spectra.

(ErO_8 and TiO_6), whereas the higher wavenumber modes are due to Ti–O stretching. The spectra could be fitted to 9 Lorentzians, marked M1 to M9 in the spectrum. Little difference between the Raman spectra of the undoped and Eu^{3+}-doped samples was observed (Fig. 3A and B), which is in agreement with the XRD results, in which both showed a pyrochlore structure. The positron lifetime studies (discussed later) also indicated that no significant defects were created by Eu^{3+}-doping in ETO. Saha et al.[25] reported Raman studies of the pyrochlore $Er_2Ti_2O_7$ at different temperatures, and the room-temperature Raman spectrum in the range of 40–800 cm^{-1} was fitted as the sum of 15 Lorentzians with support from the low temperature data. In our case, only the major peaks were considered. The obtained Raman spectra are in close agreement with the literature. Based on the literature, the various Raman modes observed in the present study were assigned to different modes as follows, although the mode accounting may involve uncertainties due to overlapping modes.[25,33–36] The M1 at 254 cm^{-1} is F_{2g}, M2 at 328 cm^{-1} is a combination of $F_{2g} + E_g$, M4 at 454 cm^{-1} is F_{2g}, M5 at 518 cm^{-1} is A_{1g} and M6 at 592 is F_{2g}. M4 at 400 cm^{-1} is attributed to E_g with M3 solely attributed to F_{2g} by Banerji et al.[37] The modes beyond M7 are due to higher order overtones or have contributions from PL.

The Raman spectra of the EZO and EEZO samples are shown in Fig. 4. The substitution of Ti in the lattice for Zr (ETO to EZO) should not significantly change the Raman spectrum, as the Raman active modes in pyrochlores are due to oxygen. Broadening of the peaks in the Raman spectra of EZO and EEZO is evident from a comparison of Fig. 4A and B. The much broader Raman spectra of EZO/EEZO compared to those of ETO/EETO is due to the defects/disordered structure of former compared to the ordered arrangement of ions in the latter. Similar changes are observed between the pyrochlore $Y_2Ti_2O_7$ and the defect fluorite structure of $Y_2Ti_{0.4}Zr_{1.6}O_7$.[38] Although the XRD patterns shows that the structures of EZO and EEZO are fluorite, some pyrochlore features are evident from the different modes shown in the figure and their comparison with the modes observed in ETO. This suggests that some pyrochlore-like local ordering is
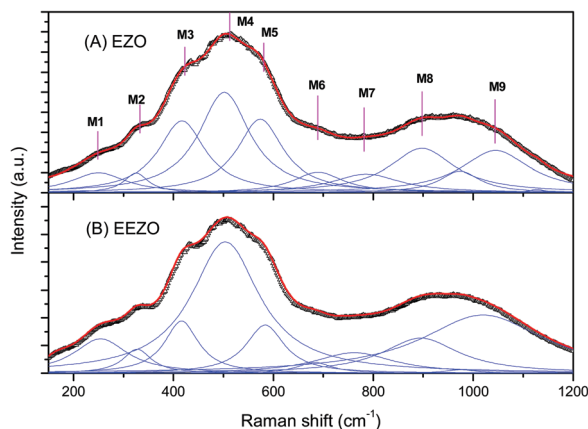
Fig. 4 Raman spectra of (A) undoped (EZO) and (B) Eu^{3+}-doped (EEZO) $Er_2Zr_2O_7$. The open symbols represent the experimental data while the solid lines are fit to the spectra.

still present in $Er_2Zr_2O_7$. This is also observed in $Y_2Sn_{2-x}Zr_xO_7$ with Zr substitution as well as the thermally induced structural evolution in $Gd_2Hf_2O_7$.[15,39] Similar short range order and the partial retention of bands attributed to pyrochlore are also observed in the supposedly fluorite-type rare earth hafnates of Dy and Yb under ambient conditions.[40]

3.4. Extended X-ray absorption fine structure

The $\chi(R)$ *vs. R* plots were generated using the $\mu(E)$ *versus E* spectra following the methodology described in ESI,† and are shown in Fig. 5a, and b for $Er_2Ti_2O_7$ and in Fig. 5c and d for $Er_2Zr_2O_7$. The structural parameters (atomic coordination and lattice parameters) of $Er_2Ti_2O_7$ and $Er_2Zr_2O_7$ used for the simulation of the theoretical EXAFS spectra of the samples

were obtained from the XRD results, and the best fit $\chi(R)$ *versus R* plots (fitting range $R = 1.0$–3.5 Å) of the samples are shown in Fig. 5a–d along with the experimental data. During the fitting, the bond distances and disorder (Debye–Waller) factors (σ^2), which give the mean square fluctuations in the distances, were used as fitting parameters and the coordination numbers were kept constant. The fitting results are tabulated in Table 1 for $Er_2Ti_2O_7$ and $Er_2Zr_2O_7$.

The Fourier transform spectrum of $Er_2Ti_2O_7$ at the Er L3 edge shows doublet peaks in the first coordination between 1.0–2.5 Å. The spectrum shown in Fourier transform space is phase-uncorrected, which shows coordination peaks slightly shifted to lower bond distances. However, during the fitting, phase correction is applied and the fitting results obtained here represent actual distances. The coordination peaks between 1.0–2.5 Å in Fig. 5a include contributions from two oxygen coordination shells at 2.18 Å and 2.42 Å, respectively, with two and six oxygen atoms in their respective coordination shell. The coordination peak at 3.0 Å is due to contributions from the next-nearest neighbour shells of Er–Zr and Er–Er at 3.49 Å and 3.58 Å, respectively. The local structure around the Ti site in $Er_2Ti_2O_7$ is different compared to that of the Er site (Fig. 5b). The Ti atoms are coordinated with a single oxygen coordination shell with six oxygens at a distance of 2.01 Å. The peak below 1 Å is due to the background noise, and was not included during the fitting. The doublet peaks between 2.5–3.75 Å are fitted with next nearest neighbour coordination shells of Ti–Er and Ti–Ti at 3.49 Å and 3.60 Å, respectively. It can be seen from the best fit values of oxygen co-ordination (*N*) given in Table 1 that significant oxygen vacancies exist near the Ti sites in the $Er_2Ti_2O_7$ sample.

The Fourier transform EXAFS spectrum of $Er_2Zr_2O_7$ at the Er L3 edge shows quite different coordination peaks from that of
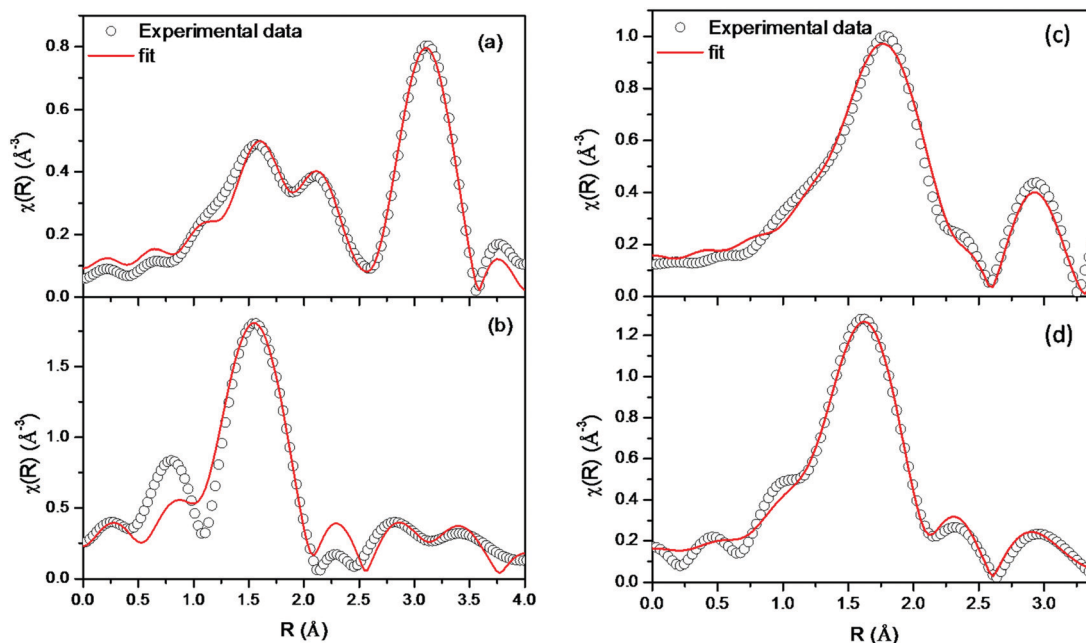

Fig. 5 Fourier-transformed EXAFS spectra of $Er_2Ti_2O_7$ at the (a) Er L3 edge and (b) Ti K-edge, and of $Er_2Zr_2O_7$ at the (c) Er L3 edge and (d) Zr K-edge.

Table 1 Bond length, coordination number, and disorder factor data obtained from EXAFS fitting at the Er L3 edge, Zr K edge, and Ti K edge. (Values in parentheses are nominal values.)

Parameter	Path	$Er_2Ti_2O_7$	$Er_2Zr_2O_7$	Path	$Er_2Ti_2O_7$	Path	$Er_2Zr_2O_7$
R (Å)	Er–O	2.18 ± 0.01	2.26 ± 0.01	Ti–O	2.01 ± 0.01	Zr–O	2.15 ± 0.01
N		2.25 ± 0.45	7.84 ± 0.76		4.98 ± 0.36		7.52 ± 0.32
		(2)	(8)		(6)		(8)
σ^2		0.0060 ± 0.0011	0.0143 ± 0.0011		0.0013 ± 0.0009		0.0048 ± 0.0009
R (Å)	Er–O	2.43 ± 0.01		Ti–Er	3.49 ± 0.01	Zr–Zr	3.45 ± 0.02
N		6.75 ± 0.90			6		6
		(6)					
σ^2		0.0163 ± 0.0010			0.0091 ± 0.0011		0.0103 ± 0.0027
R (Å)	Er–Ti/Zr	3.49 ± 0.01	3.53 ± 0.01	Ti–Ti	3.61 ± 0.02	Zr–Er	3.53 ± 0.01
N		6	6		6		6
σ^2		0.0091 ± 0.0011	0.0119 ± 0.0015		0.0029 ± 0.0016		0.0119 ± 0.0015
R (Å)	Er–Er	3.55 ± 0.02	3.59 ± 0.01				
N		6	6				
σ^2		0.0149 ± 0.0027	0.0113 ± 0.0017				

$Er_2Ti_2O_7$. This is due to the different crystal structures of $Er_2Zr_2O_7$ and $Er_2Ti_2O_7$, which were also confirmed from the XRD measurements. The Fourier transform spectrum of $Er_2Zr_2O_7$ (Fig. 5c) shows a single coordination peak as the first-nearest neighbour, which is due to contributions from eight oxygen atoms at a distance of 2.26 Å. The second peak at 3.0 Å has contributions from Er–Zr and Er–Er coordination shells at 3.52 Å and 3.59 Å, respectively. Since the Er and Zr atoms are occupying the same positions in unit cell, which leads to the same coordination geometry, the Fourier transform spectra shown in Fig. 5c and d are quite similar to each other. The first peak at the Zr K edge is due to the eight oxygen atoms at a bond distance of 2.15 Å. This Zr–O bond length is smaller than the Er–O bond length due to the difference in the ionic radii of the eight-coordinated Er^{3+} and Zr^{4+}.[41] The second coordination peak at the Zr K edge (Fig. 5d) has contributions from the Zr–Zr and Zr–Er coordination shells at 3.45 Å and 3.52 Å, respectively. Table 1 shows that the possibilities of oxygen vacancies are also greater at the Zr sites than at the Er sites for the $Er_2Zr_2O_7$ sample.

3.5. Positron annihilation studies

The positron annihilation lifetime spectra of all the samples could be fitted as the sum of three lifetime components using PALSFit, with the longest-lived component in all cases being less than 0.5% and having a lifetime of 1 to 1.5 ns. This was attributed to positronium formation on the powder surfaces and is not discussed. The other two lifetime components and their relative intensities are given in Table 2. Two components are present in all the samples, with τ_1 being lower than the bulk lifetime and τ_2 corresponding to the partial trapping of

positrons in defect states. The fractional intensity corresponding to the second lifetime component is an indication of the concentration of positrons trapped in the defects or the concentration of defects itself for similar trapping rates in the defects. A similar enhancement in I_2 with increasing defect concentration has previously been reported in bismuth-based pyrochlores.[42] The intensity-weighted average positron lifetimes were also calculated and are given in Table 2.

The presence of the second lifetime component of approximately 260 ps and significant intensity in both ETO and EETO indicates the presence of a large concentration of defects. The differences between the positron lifetimes of ETO and EETO are insignificant, showing only a marginal reduction in I_2 or a minor reduction in the concentration of defects. The two lifetimes and average lifetimes in EZO differ from those of ETO, as the structure of EZO differs from that of ETO, as seen from XRD. The average lifetime in EZO is close to that of the single positron component reported by Greg et al. in $Gd_2Zr_2O_7$.[43] The intensity of the second component is still large in EZO. This intensity is reduced significantly with an increase in the lifetime in EEZO. This shows that either the concentration of defects decreased significantly, or the type of defects changed so significantly that the positrons are not trapped in the defects of EEZO. It was seen that τ_2 also increased from 223 ps in EZO to 342 ps in EEZO, representing the possible agglomeration of vacancies into large-sized defect clusters in EEZO which appear to be low concentration. The PL emission results (discussed later) are in agreement with the assessment of defects in these samples via positron annihilation studies.

3.6. Photoluminescence studies

The emission spectrum of ETO with 250 nm excitation is shown in Fig. 6A. The emission spectrum consists of various bands and could be fitted with at least four bands centred at 430, 490, 550 and 608 nm. A small shoulder appeared at approximately 390 nm in the broad band centred at 430 nm, and the intensity of emission falls sharply below this wavelength. The emission wavelength is close to the band gap measured in $Er_2Ti_2O_7$ and other titanate-based pyrochlores.[44] The 430 nm band is attributed to defect-induced emission contributed by various

Table 2 Positron annihilation lifetimes and intensities in undoped and Eu^{3+}-doped $Er_2Ti_2O_7$ and $Er_2Zr_2O_7$
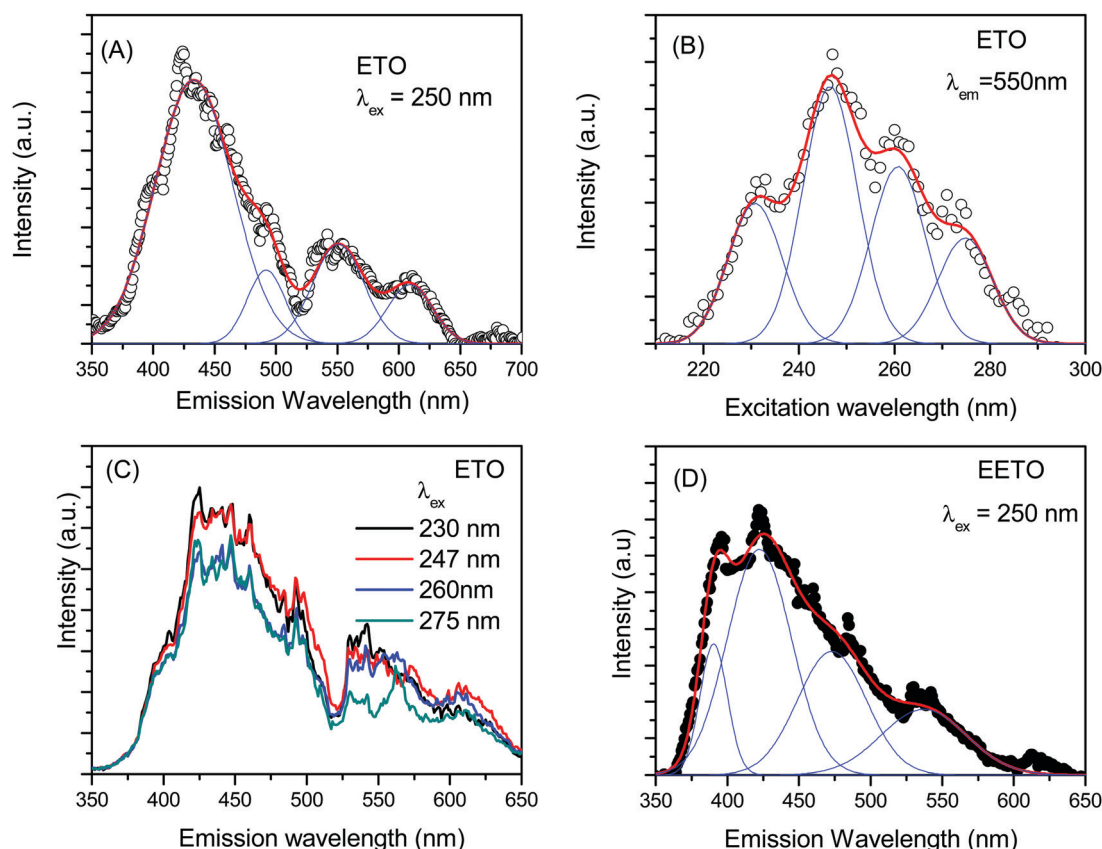
Sample	τ_1 (ps)	I_1 (%)	τ_2 (ps)	I_2 (%)	τ_{ave} (ps)
ETO	157 ± 15	22.7 ± 1.2	265 ± 5	77.1 ± 1.2	240 ± 6
EETO	151 ± 14	24.0 ± 1.2	261 ± 5	75.9 ± 1.2	234 ± 6
EZO	106 ± 11	16.3 ± 0.9	223 ± 3	83.4 ± 1.0	204 ± 4
EEZO	198 ± 4	90.2 ± 0.9	342 ± 5	9.5 ± 0.3	212 ± 5

oxygen-related defects whose energy levels lie just below the conduction band in these pyrochlores; this band is the most intense among those observed in the present studies.[18] The large concentration of defects in ETO is evident from positron annihilation lifetime spectroscopy, as indicated by the high intensity I_2 of positron annihilation from the defect states, and the EXAFS measurements at the Ti K-edge also support this. The 550 nm band represents a combination of nearby transitions in Er^{3+}, namely, $^2H_{11/2} \rightarrow {}^4I_{15/2}$ and $^4S_{3/2} \rightarrow {}^4I_{15/2}$, while that 490 nm is due to $^4F_{7/2} \rightarrow {}^4I_{15/2}$.[25,45] The origin of the small peak at approximately 610 nm is not very clear, but it is close to the emission from the $^4F_{7/2}$ level of Er^{3+} observed as a band near 625 nm by Mondal *et al.*[46] Various emission peaks from the electronic transitions in Er^{3+} appear as a broad band due to the crystal field splitting of the ground state due to the field of the surrounding oxygen atoms.[47] The excitation spectrum of ETO with the emission fixed at 550 nm is shown in Fig. 6B. It is clearly seen that multiple bands contribute to the emission, and at least four distinct bands could be observed. The bands are centred at 231, 247, 261 and 275 nm. The emission spectra were recorded with an excitation wavelength near each band, and the recorded spectra are shown in Fig. 6C. No noticeable differences were observed except for small changes in the relative intensities of the different bands discussed above, and the emission map with

varying excitation wavelength was not studied further. The emission spectrum of Eu^{3+}-doped ETO is shown in Fig. 6D. The four fitted bands are centred at 390, 425, 475 and 540 nm. The first band at 390 nm appears as a shoulder in the emission of ETO, but could be fitted as peak due to the lower intensity of the overlapping band at 425 nm compared to the corresponding band due to defect-induced emission in ETO. No specific indication of the emission from Eu^{3+} is observed. The other two bands at 475 nm and 540 nm originate from electronic transitions in Er^{3+}. However, the overlap of small intensities from the emission from Eu^{3+} in the bands ascribed to Eu^{3+} could lead to variations in the centroids of the bands determined in the EETO samples in addition to the uncertainty in fitting the bands.

The emission spectrum of $Er_2Zr_2O_7$ with excitation at 250 nm is shown in Fig. 7A. As in the case of ETO, the emission spectrum could be fitted as the sum of four bands. The four bands obtained here are centred at 425, 485, 545, and 605 nm. The emission spectra are very much similar to that of ETO, including a shoulder on the band at 425 nm, but with small shifts in the peak positions. The origin of the different bands is as discussed above. The small changes in the peak positions of the emission bands between ETO and EZO are due to the change from Ti to Zr and the resulting changes in the defect energy levels and crystal field splitting, *etc.* Even in this case,

Fig. 6 (A) The PL emission spectrum of $Er_2Ti_2O_7$ with λ_{ex} of 250 nm. The open symbols represent experimental data, while the line represents the fitting. (B) The excitation spectrum of $Er_2Ti_2O_7$ with λ_{em} of 550 nm. The open symbols represent experimental data, while the line represents the fitting. (C) Emission spectra of $Er_2Ti_2O_7$ with different excitation wavelengths. (D) The emission spectrum of Eu^{3+}-doped $Er_2Ti_2O_7$ with λ_{ex} of 250 nm. The open symbols represent experimental data while the line represents the fitting.

Fig. 7 (A) The PL emission spectrum of $Er_2Zr_2O_7$ with λ_{ex} of 250 nm. The open symbols represent experimental data, while the line represents the fitting. (B) The excitation spectrum of $Er_2Zr_2O_7$ with λ_{em} at 550 nm. The open symbols represent experimental data, while the line represents the fitting. (C) The emission spectrum of Eu^{3+}-doped $Er_2Zr_2O_7$ with λ_{ex} of 250 nm. The open symbols represent experimental data while the line represents the fitting.

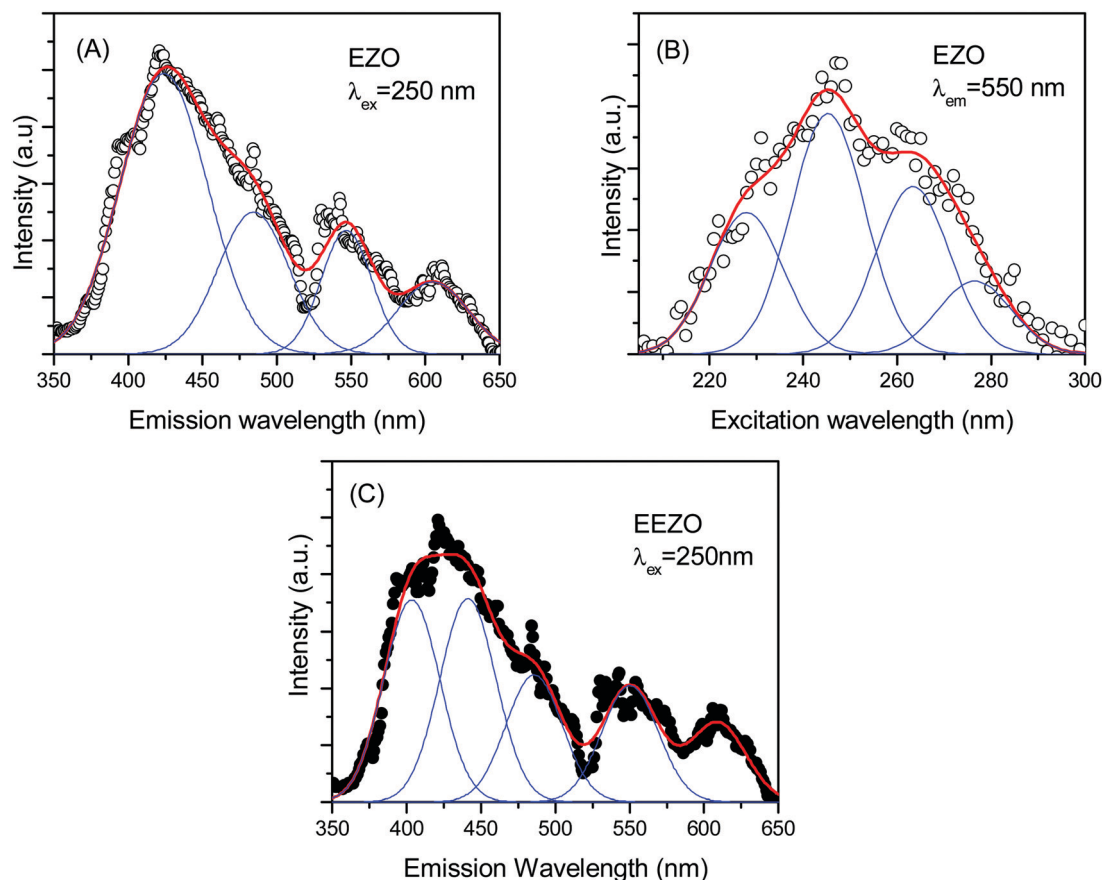the band at 425 nm is the dominant band. The excitation spectrum of EZO with emission at 550 nm is given in Fig. 7B. Like in the case of ETO, the excitation spectrum consists of multiple excitation bands and could be easily resolved into four bands centred at 228, 245, 263 and 277 nm. The splitting of the conduction band into sub-bands has been shown in the density functional theory calculations of the electronic structure in various $A_2Ti_2O_7$ (A = lanthanide) compounds.[48] Minor changes in the band positions in the excitation spectrum are due to changes in the energy levels in the band structure due to the involvement of Zr 4d levels instead of Ti 3d. The emission spectrum of Eu^{3+}-doped EZO (EEZO) is shown in Fig. 7C. The emission spectrum beyond 510 nm comprising bands at approximately 550 and 610 nm from transitions from various levels in Er^{3+} is identical to that in EZO. In the first broad band, the shoulder at the lower wavelength side could be extracted as a separate peak due to the lower intensity of the defect emission band. The band centred at 485 nm attributed to emission from the $^4F_{7/2}$ state of Er^{3+} remains, but the other defect band centred at 425 nm in EZO appears as two peaks centred at 403 and 441 nm. This is an artefact of fitting arising due to the lowering in the intensity of the 425 nm band due to changes in the defect types in Eu^{3+}-doped $Er_2Zr_2O_7$, as seen in the positron annihilation studies discussed earlier.

The emission lifetime spectra for the emission at 425 nm were recorded for all the samples and are given in Fig. 8. All the lifetime spectra yielded a single lifetime except for that of EETO, in which a small fraction of a long-lived component is observed. However, it is noted that the average lifetime in this case is in the same range as those of the other samples; the individual lifetime values are given in the figure. There is a marginal reduction in the emission lifetimes of the Eu^{3+}-doped samples with respect to the undoped ones, possibly due to the opening of the emission channels of Eu^{3+}. The intensity of the contribution from Eu^{3+} was too low to be deciphered from the other emissions, and also resulted in only minimal changes in the emission lifetimes. For the samples, the lifetimes were approximately 9–12 μs, which indicates the involvement of ionized vacancies in the photoluminescence process. The exact nature of the defects involved in the PL of EZO and ETO is confirmed using DFT calculations in the next section.

3.7. Origin of PL in ETO and EZO: DFT calculations of defect energetics

The cations in the ideal fluorite structure are eight-coordinated (A_4O_8), while the disordered defect-fluorite structure has A_4O_7. Even though the unit cell is still cubic, one of the oxygen positions is vacant and each cation is coordinated with seven

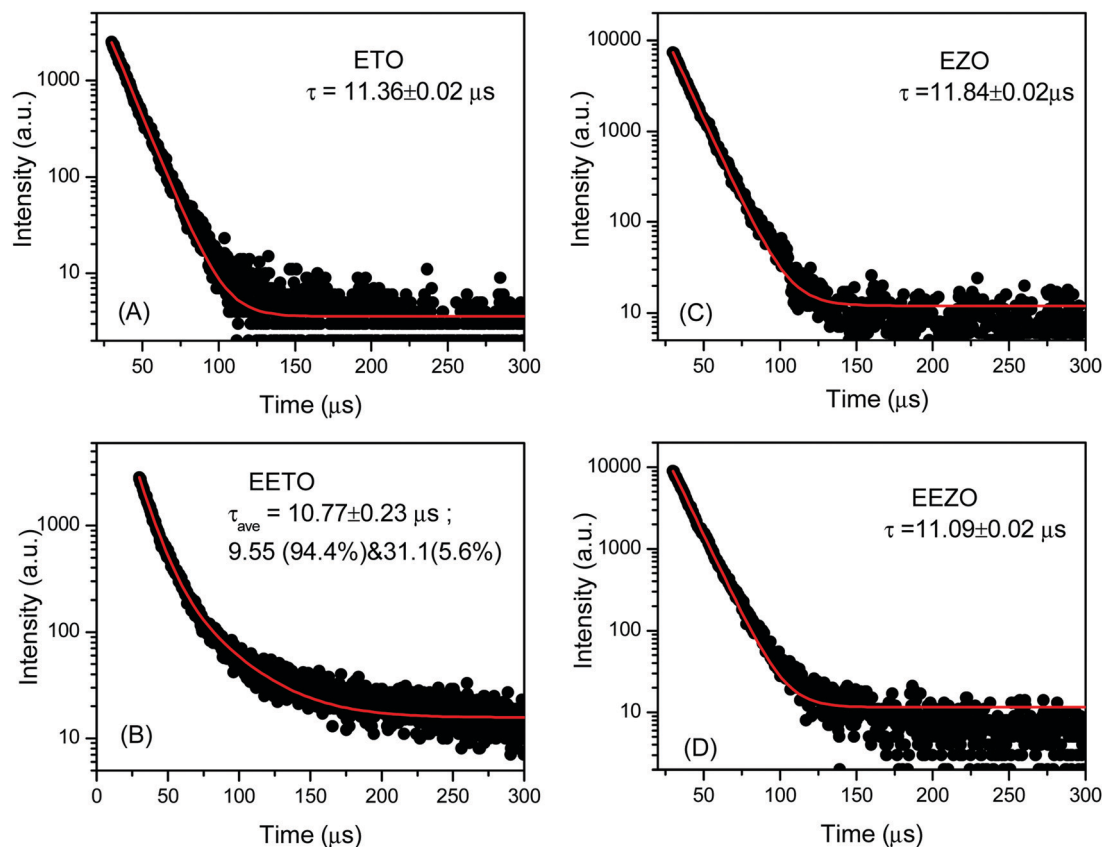**Fig. 8** PL lifetime spectra of (A) $Er_2Ti_2O_7$, (B) Eu^{3+}-doped $Er_2Ti_2O_7$, (C) $Er_2Zr_2O_7$, and (D) Eu^{3+}-doped $Er_2Zr_2O_7$ with λ_{ex} of 250 nm and λ_{em} of 425 nm. The fitting of the spectra and the emission lifetimes obtained are also indicated in the figure.

Table 3 DFT-GGA calculated structural parameters of ETO and EZO compared to experimental data and previously calculated DFT results

Property	$Er_2Ti_2O_7$, ETO (ordered pyrochlore)	$Er_2Zr_2O_7$, EZO (disordered fluorite)
Lattice parameter (Å)	10.119 (10.0762,[49] 10.071[51])	5.2725 (5.193(2),[50] 5.1822 [This work])
ErO_8 bond lengths (Å)	2.30–2.56 (2.182, 2.471[49])	2.13–2.49
TiO_6/ZrO_6 bond lengths (Å)	2.11–2.15 (1.955[49])	1.99–2.91
x of O_{48f}	0.332 (0.420,[49] 0.328[51])	—
Band gap (eV)	3.0 (3.0[51])	3.2

Fig. 9 GGA calculated oxygen defect formation energy (E_f) versus Fermi level (E_F) for the three charge states, V_q^0, V_q^{+1}, and V_q^{+2}, in EZO and ETO (left panel). The defect exhibits two charge-state transition levels: a deep donor level, $\varepsilon(+2/+1)$, at 2.30 and 2.65 eV for EZO and ETO, respectively, and another deep donor level, $\varepsilon(+1/0)$, at 3.00 and 2.80 eV for EZO and ETO, respectively. The obtained impurity levels are shown in a conventional band diagram with respect to the host referred binding energies (HRBE) (right panel).

anions. ETO stabilizes in the ordered pyrochlore structure and EZO stabilizes in the disordered fluorite structure. Our DFT-GGA calculated equilibrium lattice parameters of ETO and EZO are compared with experimental data[49,50] and previous DFT calculations[51] (Table 3). The DFT-GGA calculated lattice

parameters and bond lengths of ETO are within 1% and 5% of the experimental values, respectively. Moreover, our DFT-GGA calculated values are in excellent agreement with previous DFT calculations using the full potential linear augmented plane wave (FP-LMTO) method.[51] Our DFT-GGA calculated lattice

Fig. 10 Total and partial density of states (DOS) of Eu-doped ETO in the presence of a neutral oxygen vacancy (V_O^0) (a), an oxygen vacancy of charge +1 (V_O^{+1}) (b), and an oxygen vacancy of charge +2 (V_O^{+2}) (c). Similarly, the total and partial DOS of Eu-doped EZO in the presence of a neutral oxygen vacancy (V_O^0) (d), an oxygen vacancy of charge +1 (V_O^{+1}) (e), and an oxygen vacancy of charge +2 (V_O^{+2}) (f). Fermi energies are shown as vertical lines.

parameter for EZO is within 1.5% of the experimentally measured value.

In order to determine the effect of the oxygen vacancies on the photoluminescence properties, defect formation energies in various charge states (V_O^0, V_O^{+1} and V_O^{+2}) were calculated. The oxygen vacancies can be located in the ErO_8 or TiO_6 polyhedra. In order to find the most energetically favourable location for the oxygen vacancy, two calculations having a neutral oxygen vacancy (V_O^0) were performed, in which the vacant oxygen site was chosen in the first nearest-neighbour of the ErO_8 and TiO_6 polyhedra. Our DFT-GGA calculated defect energetics indicated that the introduction of a neutral oxygen vacancy is preferable in the TiO_6 octahedra compared to the ErO_8 polyhedra, with a vacancy formation energy difference of 2.47 eV. A similar exercise was performed for EZO and it was found that the oxygen vacancy was more favourable in the first nearest neighbour of Zr. To see how the defect formation energies of the oxygen vacancies in the dilute limit varied as a function of the Fermi energy, we have summarized the DFT-calculated formation energies of ETO and EZO in Fig. 9 (left panel). The calculated vacancy formation energy values indicate that the formation of V_O^{+2} defects is favoured in near the valence band in the 0 to 2.65 eV and 0 to 2.30 eV range (on the E_F–E_V scale) for ETO and EZO, respectively, over V_O^{+1} and V_O^0 defects. This indicates that the oxygen vacancies have a tendency to donate electrons or behave as a n-type defect. Similarly, the formation of V_O^{+1} defects is most favourable in the 2.65 to 2.80 eV and 2.30 eV to 3.0 eV ranges (on the E_F–E_V scale) for ETO and EZO, respectively, followed by formation of V_O^0 defects. The DFT-GGA calculated electronic band gaps of ETO and EZO are 3.0 eV and 3.2 eV, respectively. We are unable to compare these band gap values as no experimental band gap has been reported in the literature. However, the previous FP-LMTO calculated band gap of ETO matches exactly with our DFT-GGA calculated value.

Fig. 9 (right panel) shows that the defect exhibits two charge-state transition levels: a deep donor level $\varepsilon(+2/+1)$ at 2.65 eV and 2.30 eV for ETO and EZO, respectively, and another deep donor level $\varepsilon(+1/0)$ at 2.8 eV and 3.0 eV for ETO and EZO, respectively. In this case, the impurity levels are defined as the charge-state transition levels ($\varepsilon(q_1/q_2)$, from q_1 to q_2), i.e., the Fermi level locations at which the two charge states of the defect have the same formation energy. The obtained impurity levels are shown in a conventional band diagram with respect to the host referred binding energies (HRBE). The charge-state transition level situated at 2.80 eV and 3.0 eV, respectively, for ETO and EZO corresponds to wavelengths of 443 and 413 nm. The experimental photoluminescence emission spectra show a bright emission band at 430 nm and 425 nm, respectively. The DFT-GGA calculated charge transition levels qualitatively explain the origin of the brightest spectral feature of ETO and EZO.

3.8. No europium emission in EEZO and EETO: density of state calculations

In our calculations, we considered a 1/88 (1.136%) Eu doping level in the defective cells of ETO and EZO in order to determine the effect of Eu doping on the photoluminescence properties of ETO and EZO. Previously, it was explained that the photoluminescence properties of ETO and EZO are dominated by neutral and/or charged oxygen-defect-related states. Fig. 10 shows the total and partial density of states (DOS) of Eu-doped ETO and EZO in the presence of a neutral oxygen vacancy (V_O^0), oxygen vacancy of charge +1 (V_O^{+1}) and oxygen vacancy of charge +2 (V_O^{+2}). Initially, two sets of calculations were performed in which the Eu atom was doped in the Er and Ti/Zr positions and the atomic positions were optimized keeping the volume and lattice shape fixed. It was found that Eu atom doped at the Er position was more energetically stable. The DOS shown in Fig. 10 were generated by doping the Eu atom at the Er position. Fig. 10 shows that the Eu f-states are dominantly distributed around the bottom edge of the valence band (VB) far from the Fermi energy, electronic band gap and top edge of the VB actively participating in the electronic transitions. Similarly, the Eu f-states are distributed around the top edge of the conduction band away from the electronic band-gap region. As a result, the active participation of the Eu-f states in electronic transitions giving rise to photoluminescence emission is impossible. This is also corroborated by the fact that the experimental photoluminescence emission of ETO and EZO was scarcely affected by Eu doping.

4. Conclusions

In this work, undoped and doped EZO, ETO, EEZO, and EETO microcrystals with differing structures, defects, and ordering were synthesized using a ball-milling method. Rietveld-refined XRD and Raman spectroscopy confirmed the stabilization of undoped and doped ETO/EETO in the ordered pyrochlore structure and of EZO/EEZO in the defect fluorite structure. Synchrotron-based EXAFS measurements and PALS suggested a large concentration of defects in both samples, although the nature and concentration of defects in the zirconium material were quite different than in the titanium counterpart, with the possible formation of defect agglomerates and clusters in the former. Based on the PALS results, the effect of europium in defect evolution was found to be negligible for ETO, whereas it was substantial in the case of EZO. The undoped EZO and ETO hosts exhibited blue photoluminescence under UV light with a few weaker trivalent Er^{3+} spectral features in the green-yellow-red zone also. XANES studies confirmed that Ti and Zr stabilize in the +4 oxidation state, ruling out any contributions from trivalent Zr^{3+} and Ti^{3+} to the PL of EZO and ETO. The intense blue emission of ETO and EZO was ascribed to OVs, which were experimentally probed using EXAFS, and furthermore, the actual transitions involving OVs were confirmed using DFT calculated energetics. No characteristic europium emission was observed after europium doping, which was quite unexpected and interesting. The density of states calculations clearly suggest a mismatch between the Eu^{3+} f-state and the host band gap, inhibiting any kind of host-to-dopant energy transfer, and, hence, no red europium PL was observed. This work

demonstrates the role of energy transfer, the band gap, and the choice of host and dopant in optimizing the optical properties of lanthanide-doped pyrochlore phosphors for efficient optoelectronics and scintillator applications.

Conflicts of interest

There are no conflicts of interest to declare.

References

1 K. Alberi, M. B. Nardelli, A. Zakutayev, L. Mitas, S. Curtarolo, A. Jain, M. Fornari, N. Marzari, I. Takeuchi, M. L. Green, M. Kanatzidis, M. F. Toney, S. Butenko, B. Meredig, S. Lany, U. Kattner, A. Davydov, E. S. Toberer, V. Stevanovic, A. Walsh, N.-G. Park, A. Aspuru-Guzik, D. P. Tabor, J. Nelson, J. Murphy, A. Setlur, J. Gregoire, H. Li, R. Xiao, A. Ludwig, L. W. Martin, A. M. Rappe, S.-H. Wei and J. Perkins, The 2019 materials by design roadmap, *J. Phys. D: Appl. Phys.*, 2018, **52**, 013001.

2 K. Khan, A. K. Tareen, M. Aslam, R. Wang, Y. Zhang, A. Mahmood, Z. Ouyang, H. Zhang and Z. Guo, Recent developments in emerging two-dimensional materials and their applications, *J. Mater. Chem. C*, 2020, **8**, 387–440.

3 J. Luo, X. Wang, S. Li, J. Liu, Y. Guo, G. Niu, L. Yao, Y. Fu, L. Gao, Q. Dong, C. Zhao, M. Leng, F. Ma, W. Liang, L. Wang, S. Jin, J. Han, L. Zhang, J. Etheridge, J. Wang, Y. Yan, E. H. Sargent and J. Tang, Efficient and stable emission of warm-white light from lead-free halide double perovskites, *Nature*, 2018, **563**, 541–545.

4 K. Richardson, M. Kang, L. Sisken, A. Yadav, C. Blanco, M. Antia, S. Novak, C. Smith, A. Buff and A. Lepicard, Advances in infrared GRIN: a review of novel materials towards components and devices, *Advanced Optics for Defense Applications: UV through LWIR III, International Society for Optics and Photonics*, 2018, p. 106270A.

5 B. B. Srivastava, S. K. Gupta and Y. Mao, Single red emission from upconverting $ZnGa_2O_4$:Yb,Er nanoparticles co-doped by Cr^{3+}, *J. Mater. Chem. C*, 2020, **8**, 6370–6379.

6 C. Sun, K. Li and D. Xue, Searching for novel materials *via* 4f chemistry, *J. Rare Earths*, 2019, **37**, 1–10.

7 A. P. Anantharaman and H. P. Dasari, Potential of pyrochlore structure materials in solid oxide fuel cell applications, *Ceram. Int.*, 2020, **47**(4), 4367–4388.

8 Q. Deng, R. Gao, X. Li, J. Wang, Z. Zeng, J.-J. Zou and S. Deng, Hydrogenative Ring-Rearrangement of Biobased Furanic Aldehydes to Cyclopentanone Compounds over Pd/Pyrochlore by Introducing Oxygen Vacancies, *ACS Catal.*, 2020, **10**, 7355–7366.

9 S. K. Gupta, J. P. Zuniga, M. Abdou, M. P. Thomas, M. D. A. Goonatilleke, B. S. Guiton and Y. Mao, Lanthanide-doped lanthanum hafnate nanoparticles as multicolor phosphors for warm white lighting and scintillators, *Chem. Eng. J.*, 2020, **379**, 122314.

10 M. A. Sullivan, D. Stenger, A. Roma and M. Tynan, The future of nuclear power, *Electr. J.*, 2014, **27**, 7–15.

11 A. Horvath and E. Rachlew, Nuclear power in the 21st century: Challenges and possibilities, *Ambio*, 2016, **45**, 38–49.

12 N. C. Hyatt and M. I. Ojovan, *Materials for Nuclear Waste Immobilization*, Multidisciplinary Digital Publishing Institute, 2019.

13 F. Angeli, T. Charpentier, P. Jollivet, D. de Ligny, M. Bergler, A. Veber, S. Gin and H. Li, Effect of thermally induced structural disorder on the chemical durability of International Simple Glass, *npj Mater. Degrad.*, 2018, **2**, 31.

14 M. Abdou, S. K. Gupta, J. P. Zuniga and Y. Mao, On structure and phase transformation of uranium doped $La_2Hf_2O_7$ nanoparticles as an efficient nuclear waste host, *Mater. Chem. Front.*, 2018, **2**, 2201–2211.

15 S. K. Gupta, M. Abdou, P. S. Ghosh, J. P. Zuniga and Y. Mao, Thermally Induced Disorder–Order Phase Transition of $Gd_2Hf_2O_7$:Eu^{3+} Nanoparticles and Its Implication on Photo- and Radioluminescence, *ACS Omega*, 2019, **4**, 2779–2791.

16 S. K. Gupta, P. Ghosh, C. Reghukumar, N. Pathak and R. Kadam, Experimental and theoretical approach to account for green luminescence from $Gd_2Zr_2O_7$ pyrochlore: exploring the site occupancy and origin of host-dopant energy transfer in $Gd_2Zr_2O_7$:Eu^{3+}, *RSC Adv.*, 2016, **6**, 44908–44920.

17 S. K. Gupta, K. Sudarshan, P. S. Ghosh, A. P. Srivastava, S. Bevara, P. K. Pujari and R. M. Kadam, Role of various defects in the photoluminescence characteristics of nanocrystalline $Nd_2Zr_2O_7$: an investigation through spectroscopic and DFT calculations, *J. Mater. Chem. C*, 2016, **4**, 4988–5000.

18 S. K. Gupta, M. Abdou, P. S. Ghosh, J. P. Zuniga, E. Manoharan, H. Kim and Y. Mao, On comparison of luminescence properties of $La_2Zr_2O_7$ and $La_2Hf_2O_7$ nanoparticles, *J. Am. Ceram. Soc.*, 2020, **103**, 235–248.

19 L. Zhang, W. Zhang, J. Zhu, Q. Hao, C. Xu, X. Yang, L. Lu and X. Wang, Synthesis of $Er_2Ti_2O_7$ nanocrystals and its electrochemical hydrogen storage behavior, *J. Alloys Compd.*, 2009, **480**, L45–L48.

20 J. Gaudet, A. M. Hallas, J. Thibault, N. P. Butch, H. Dabkowska and B. Gaulin, Experimental evidence for field-induced emergent clock anisotropies in the XY pyrochlore $Er_2Ti_2O_7$, *Phys. Rev. B*, 2017, **95**, 054407.

21 N. B. Amor, M. Bejar, M. Hussein, E. Dhahri, M. Valente and E. Hlil, Synthesis, Magnetic Properties, Magnetic Entropy and Arrot Plot of Antiferromagnetic Frustrated $Er_2Ti_2O_7$ Compound, *J. Supercond. Novel Magn.*, 2012, **25**, 1035–1042.

22 M. Martos, B. Julián-López, E. Cordoncillo and P. Escribano, Structural and spectroscopic study of a new pink chromium-free $Er_2(Ti,Zr)_2O_7$ ceramic pigment, *J. Am. Ceram. Soc.*, 2009, **92**, 2987–2992.

23 M. Langlet, C. Coutier, J. Fick, M. Audier, W. Meffre, B. Jacquier and R. Rimet, Sol–gel thin film deposition and characterization of a new optically active compound: $Er_2Ti_2O_7$, *Opt. Mater.*, 2001, **16**, 463–473.

24 M. Langlet, P. Jenouvrier, R. Rimet and J. Fick, Aerosol–gel deposition and spectroscopic characterization of pyrochlore films heavily doped with erbium ions, *Opt. Mater.*, 2004, **25**, 141–147.

25 S. Saha, S. Prusty, S. Singh, R. Suryanarayanan, A. Revcolevschi and A. Sood, Anomalous temperature dependence of phonons and photoluminescence bands in pyrochlore $Er_2Ti_2O_7$: signatures of structural deformation at 130 K, *J. Phys.: Condens. Matter*, 2011, **23**, 445402.

26 H. Arfin, J. Kaur, T. Sheikh, S. Chakraborty and A. Nag, Bi3+–Er3+ and Bi3+–Yb3+ Codoped Cs2AgInCl6 Double Perovskite Near-Infrared Emitters, *Angew. Chem., Int. Ed.*, 2020, **59**, 11307–11311.

27 W. J. Mir, T. Sheikh, H. Arfin, Z. Xia and A. Nag, Lanthanide doping in metal halide perovskite nanocrystals: spectral shifting, quantum cutting and optoelectronic applications, *NPG Asia Mater.*, 2020, **12**, 9.

28 G. Pan, X. Bai, D. Yang, X. Chen, P. Jing, S. Qu, L. Zhang, D. Zhou, J. Zhu, W. Xu, B. Dong and H. Song, Doping Lanthanide into Perovskite Nanocrystals: Highly Improved and Expanded Optical Properties, *Nano Lett.*, 2017, **17**, 8005–8011.

29 M. Pokhrel, K. Wahid and Y. Mao, Systematic Studies on $RE_2Hf_2O_7$:5%Eu^{3+} (RE = Y, La, Pr, Gd, Er, and Lu) Nano-particles: Effects of the A-Site RE^{3+} Cation and Calcination on Structure and Photoluminescence, The, *J. Phys. Chem. C*, 2016, **120**, 14828–14839.

30 T. Yamamoto, Assignment of pre-edge peaks in K-edge X-ray absorption spectra of 3d transition metal compounds: electric dipole or quadrupole?, *X-Ray Spectrometry: An International Journal*, 2008, **37**, 572–584.

31 M. Sahoo, A. Yadav, S. Jha, D. Bhattacharyya, T. Mathews, N. Sahoo, S. Dash and A. Tyagi, Nitrogen location and Ti–O bond distances in pristine and N-doped TiO_2 anatase thin films by X-ray absorption studies, *J. Phys. Chem. C*, 2015, **119**, 17640–17647.

32 H. Gupta, S. Brown, N. Rani and V. Gohel, A lattice dynamical investigation of the Raman and the infrared frequencies of the cubic A2Hf2O7 pyrochlores, *J. Phys. Chem. Solids*, 2002, **63**, 535–538.

33 M. Vandenborre, E. Husson, J. Chatry and D. Michel, Rare-earth titanates and stannates of pyrochlore structure; vibrational spectra and force fields, *J. Raman Spectrosc.*, 1983, **14**, 63–71.

34 D. Arenas, L. Gasparov, W. Qiu, J. Nino, C. H. Patterson and D. Tanner, Raman study of phonon modes in bismuth pyrochlores, *Phys. Rev. B: Condens. Matter Mater. Phys.*, 2010, **82**, 214302.

35 M. Maczka, J. Hanuza, K. Hermanowicz, A. Fuentes, K. Matsuhira and Z. Hiroi, Temperature-dependent Raman scattering studies of the geometrically frustrated pyro-chlores $Dy_2Ti_2O_7$, $Gd_2Ti_2O_7$ and $Er_2Ti_2O_7$, *J. Raman Spectrosc.*, 2008, **39**, 537–544.

36 Q. Wang, A. Ghasemi, A. Scheie and S. Koohpayeh, Synthesis, crystal growth and characterization of the pyrochlore $Er_2Ti_2O_7$, *CrystEngComm*, 2019, **21**, 703–709.

37 A. Banerji, B. Mandal, T. Sairam and A. Tyagi, Pressure induced structural stability studies on $Nd_2Zr_2O_7$ pyrochlore, *Solid State Commun.*, 2011, **151**, 321–325.

38 M. Glerup, O. F. Nielsen and F. W. Poulsen, The structural transformation from the pyrochlore structure, $A_2B_2O_7$, to the fluorite structure, AO_2, studied by Raman spectroscopy and defect chemistry modeling, *J. Solid State Chem.*, 2001, **160**, 25–32.

39 M. de los Reyes, K. R. Whittle, Z. Zhang, S. E. Ashbrook, M. R. Mitchell, L.-Y. Jang and G. R. Lumpkin, The pyro-chlore to defect fluorite phase transition in Y2Sn$_{2-x}$Zr$_x$O$_7$, *RSC Adv.*, 2013, **3**, 5090–5099.

40 K. M. Turner, D. R. Rittman, R. A. Heymach, C. L. Tracy, M. L. Turner, A. F. Fuentes, W. L. Mao and R. C. Ewing, Pressure-induced structural modifications of rare-earth haf-nate pyrochlore, *J. Phys.: Condens. Matter*, 2017, **29**, 255401.

41 R. D. Shannon, Revised effective ionic radii and systematic studies of interatomic distances in halides and chalcogen-ides, *Acta Crystallogr., Sect. A: Cryst. Phys., Diffr., Theor. Gen. Crystallogr.*, 1976, **32**, 751–767.

42 H. Du, X. Yao, X. Zhang and H. Weng, Defect structure and dielectric properties of Bi-based pyrochlores probed by positron annihilation, *Appl. Surf. Sci.*, 2006, **253**, 1856–1860.

43 D. J. Gregg, Z. Zhang, G. J. Thorogood, B. J. Kennedy, J. A. Kimpton, G. J. Griffiths, P. R. Guagliardo, G. R. Lumpkin and E. R. Vance, Cation antisite disorder in uranium-doped gadolinium zirconate pyrochlores, *J. Nucl. Mater.*, 2014, **452**, 474–478.

44 R. Abe, M. Higashi, Z. Zou, K. Sayama and Y. Abe, Photo-catalytic water splitting into H_2 and O_2 over $R_2Ti_2O_7$ (R= Y, rare earth) with pyrochlore structure, *Chem. Lett.*, 2004, **33**, 954–955.

45 V. Venkatramu, S. F. León-Luis, U. R. Rodríguez-Mendoza, V. Monteseguro, F. J. Manjón, A. D. Lozano-Gorrín, R. Valiente, D. Navarro-Urrios, C. Jayasankar and A. Muñoz, Synthesis, structure and luminescence of Er^{3+}-doped Y$_3$Ga$_5$O nano-garnets, *J. Mater. Chem.*, 2012, **22**, 13788–13799.

46 K. Mondal, K. Hartman, D. Dasgupta, G. Trifon and M. Dasari, Synthesis and characterization of $Y_2Ti_2O_7$ and Er$_x$Y$_{2-x}$Ti$_2O_7$ nanofibers, *J. Sol-Gel Sci. Technol.*, 2015, **73**, 265–269.

47 B. Malkin, T. Lummen, P. Van Loosdrecht, G. Dhalenne and A. Zakirov, Static magnetic susceptibility, crystal field and exchange interactions in rare earth titanate pyrochlores, *J. Phys.: Condens. Matter*, 2010, **22**, 276003.

48 V. Nemoshkalenko, S. Borisenko, V. Uvarov, A. Yaresko, A. Vakhney, A. Senkevich, T. Bondarenko and V. Borisenko, Electronic structure of the $R_2Ti_2O_7$ (R = Sm–Er, Yb, Lu) oxides, *Phys. Rev. B: Condens. Matter Mater. Phys.*, 2001, **63**, 075106.

49 O. Knop, F. Brisse and L. Castelliz, Determination of the crystal structure of erbium titanate, $Er_2Ti_2O_7$, by X-ray and neutron diffraction, *Can. J. Chem.*, 1965, **43**, 2812–2826.

50 F. Zhang, M. Lang, U. Becker, R. Ewing and J. Lian, High pressure phase transitions and compressibilities of $Er_2Zr_2O_7$ and $Ho_2Zr_2O_7$, *Appl. Phys. Lett.*, 2008, **92**, 011909.

51 N. Deilynazar, E. Khorasani, M. Alaei and S. J. Hashemifar, First-principles insights into f magnetism: A case study on some magnetic pyrochlores, *J. Magn. Magn. Mater.*, 2015, **393**, 127–131.